Volume 28
Number 18
13 May 2026
Pages 10981–11482

# PCCP

Physical Chemistry Chemical Physics

rsc.li/pccp

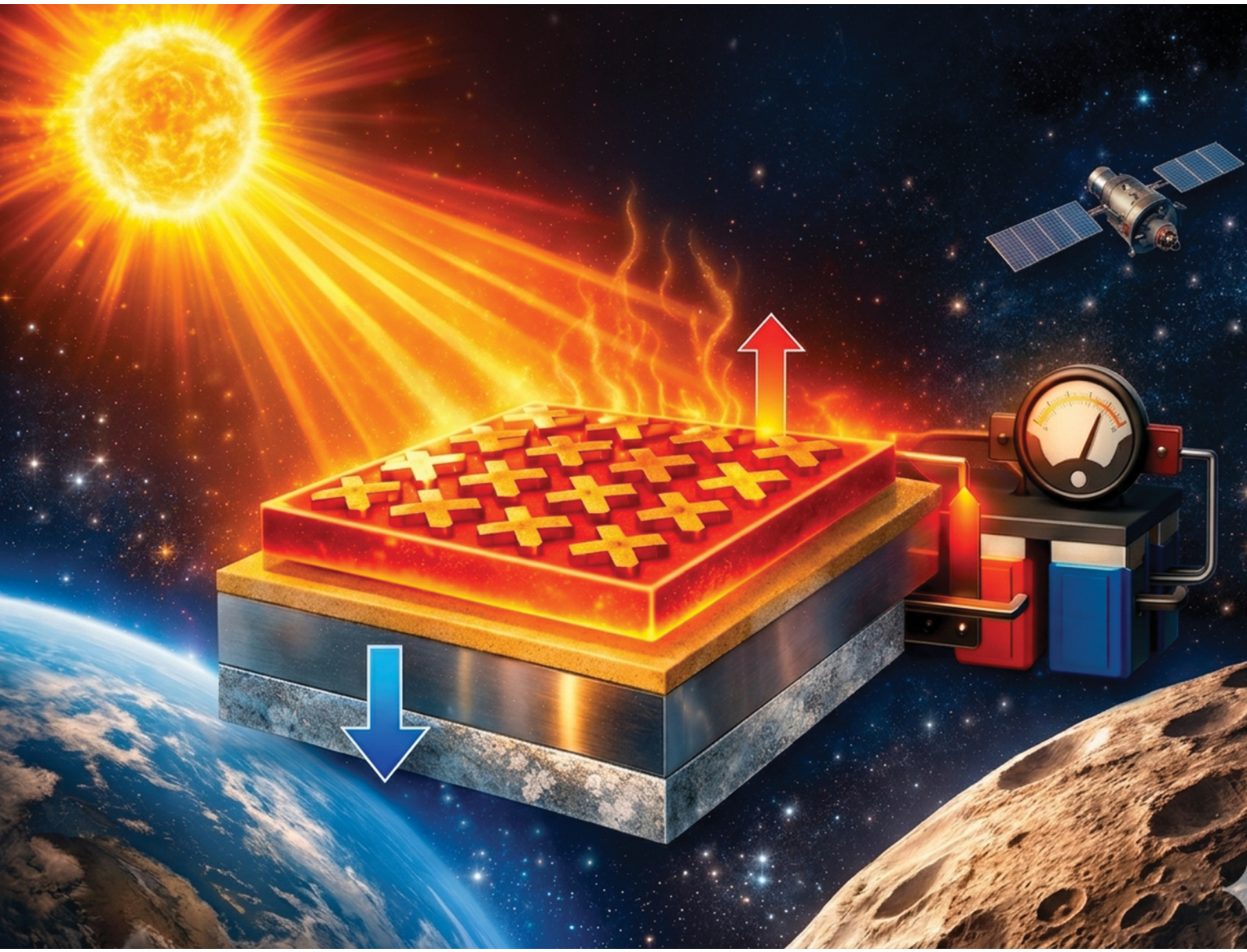

ISSN 1463-9076

ROYAL SOCIETY OF CHEMISTRY

**PAPER**

Remo Proietti Zaccaria, Shu-Jen Wang *et al.*
Near-unity broadband photonic metamaterial absorber for thermoelectric energy harvesting in Space

PCCP Owner Societies

PCCP

PAPER

View Article Online
View Journal | View Issue



Cite this: *Phys. Chem. Chem. Phys.*, 2026, **28**, 11034

# Near-unity broadband photonic metamaterial absorber for thermoelectric energy harvesting in Space

Mikita Marus,[ab] Nikolay Lyapunov,[a] Aliaksandr Hubarevich,[bc] Remo Proietti Zaccaria*[b] and Shu-Jen Wang*[a]

Spaceborne power systems must operate reliably for decades with minimal maintenance. Thermoelectric generators (TEGs) are intrinsically suited to long-lived missions, but their output remains constrained by available thermal gradients and the limitations of bulk thermoelectric materials. Here, we introduce a photonic metamaterial (PtMM) coating concept that amplifies the thermal gradient available to a TEG by converting incident AM0 solar irradiance into strongly localised photothermal energy on the TEG hot side. We design, optimise, and numerically characterise two metal–insulator–metal PtMM geometries – nanocross (NC-PtMM) and nanosquare (NS-PtMM) – using standard thin-film materials. The optimised NC-PtMM achieves near-unity peak absorptance (≈99%) and >95% average absorptance across the visible band, with strong field confinement at the resonator/spacer interface that concentrates dissipated power. Coupled electromagnetic–thermal simulations quantify (i) steady/quasi-steady temperature localisation under continuous irradiation and (ii) the intrinsic non-equilibrium photothermal response under ns-scale pulse trains used as a transient probe. The designs are effectively polarisation-insensitive at normal incidence; NS-PtMM is included as a manufacturability-motivated reference geometry, while detailed NS-PtMM optimisation is left for future work. The material stack (Cr, $Al_2O_3$, Al/$SiO_2$, and an optically thick Ag ground plane) is compatible with standard microfabrication routes, and we outline a Space-qualification screening matrix (atomic oxygen exposure, radiation/TID, and thermal-vacuum cycling). Overall, the results establish a practical pathway toward metamaterial-augmented thermoelectric harvesting for compact Space platforms (*e.g.*, CubeSats and landers) and motivate related photothermal coating concepts for spacecraft thermal management and hybrid PV-TEG harvesting.

Received 6th December 2025,
Accepted 23rd February 2026

DOI: 10.1039/d5cp04738b

rsc.li/pccp



## 1. Introduction

Long-lived, maintenance-free electrical power is a foundational requirement for many classes of Space missions – from deep-space probes and long-duration lunar platforms to distributed sensor nodes and long-lived small satellites.[1–4] Photovoltaics (PV) and radioisotope thermoelectric generators (RTGs) currently provide the bulk of civil and scientific space power, but both approaches face practical constraints. PV systems suffer from angle-dependent insolation, degradation in harsh radiation environments, and limited performance far from the Sun.[3] RTGs deliver reliable power but rely on limited isotopic resources and complex regulatory/handling constraints.[5] These limitations motivate complementary approaches that combine simplicity, durability, and scalable integration with existing spacecraft architectures.

Thermoelectric generators (TEGs) are attractive in this context because they provide solid-state conversion between a thermal gradient and electricity, have no moving parts, and allow for decades of operation with minimal maintenance.[6–9] In Space settings, TEGs are already deployed in RTGs, and there is growing interest in using thermoelectrics for non-isotopic thermal harvesting (*e.g.*, waste-heat recovery, environment-driven thermal differentials, and various hybrid architectures for CubeSats).[10–12] Nevertheless, achievable power densities from conventional TEGs remain limited by (i) the magnitude of available temperature differences at the TEG hot and cold interfaces, and (ii) intrinsic material trade-offs (Seebeck coefficient *vs.* electrical/thermal conductivity) that limit the figure-of-merit, $ZT$,

[a] *Department of Physics, Hong Kong Baptist University, Kowloon Tong, Kowloon, Hong Kong. E-mail: shu-jenwang@hkbu.edu.hk*
[b] *Istituto Italiano di Tecnologia, Via Morego 30, I-16163 Genova, Italy. E-mail: remo.proietti@iit.it*
[c] *Belarusian State University of Informatics and Radioelectronics, 6 P. Brouki, Minsk 220013, Belarus*

of bulk thermoelectric materials.[13,14] Continued progress in material chemistry improves *ZT*, but many missions would benefit from strategies that increase the accessible thermal gradient without requiring the development of new thermoelectric chemistries.[15]

Metamaterial (MM) and metasurface absorbers offer such a strategy.[16–18] Metal–insulator–metal (MIM) and related metasurface designs offer a near-complete control of reflectance, transmittance, and absorptance *via* subwavelength patterning.[16–22] From the perspective of power for Space, MM absorbers can be engineered to concentrate incident electromagnetic power into ultrathin volumes, while being mechanically simple. This concentration can be tailored to the top side of a TEG hotplate, producing locally enhanced temperature at the hot contact and therefore increasing the effective $\Delta T$ the TEG can harvest – all without changing the thermoelectric leg materials or module architecture.[23] Seminal demonstrations and reviews establish the underlying design rules (impedance matching, resonant field localization, MIM Fabry–Pérot/*meta*-cavity engineering) and practical implementation methods.

Recent theoretical and experimental work directly connects MM absorbers to thermoelectric enhancement.[23,24] Optics-thermal coupling studies show that MIM absorbers and plasmonic metasurfaces can produce strong localised heating that propagates into conventional thermoelectric legs, increasing the harvested voltage and power under uniform irradiance conditions.[23–27] A growing number of publications demonstrate improved photo-thermoelectric response when an MPA (metamaterial perfect absorber) or metasurface is used as the photon-to-heat interface.[28–31] These studies indicate that properly designed metamaterials can increase usable thermal gradients even when illuminated by broadband solar spectra relevant to Space (AM0).

Operating in Space strongly constrains the choice of materials and fabrication methods.[32,33] Space-facing coatings must withstand thermal cycling, UV exposure, charged-particle radiation, and, in low-Earth orbit, atomic-oxygen erosion.[34–36] Therefore, designs that use materials and processes already established in semiconductor and aerospace manufacturing – for example, Al, Cr, Ag, Ni, common dielectric spacers ($Al_2O_3$, $SiO_2$), and industry-standard lithography or templated deposition techniques – reduce development risk and accelerate qualification for flight.[37] These practical considerations make MM augmentation a realistic near-term option for boosting TEG performance in Space missions.

In this work, we propose a MM coating concept for flight-ready TEG modules aimed at long-duration platforms (for example, CubeSats and planetary landers) that substantially increases the thermal gradient available to a thermoelectric leg under AM0 illumination. The designs are intentionally constrained to industry-proven thin-film materials and standard microfabrication workflows to facilitate rapid translation to module-level testing and Space qualification. We present the design rules, full-wave absorptance spectra, interface-resolved field maps, volumetric Joule heating distributions, and transient electromagnetic-thermal coupling that together establish the nanocross PtMM (NC-PtMM) and nanosquare PtMM (NS-PtMM) as practical photothermal coatings for TEG augmentation. We also report fabrication feasibility and recommended Space-qualification testing to support translation to flight.

## 2. Structure design and methods

### 2.1 Design rationale

- Use a MIM photonic metamaterial (limited by three to five layers) enabling impedance matching to free space and strong field localisation (*meta*-cavity/Fabry–Pérot type behaviour).[16,38–42]
- Prioritise broadband absorptance across 300–2000 nm (visible & NIR-I/II) to capture the majority of AM0 spectral power ($\approx$1361 W m$^{-2}$ integrated).[43,44]
- Limit stack complexity ($\leq$5 layers) and choose constituent materials common in semiconductor fabs (Cr, Al, $Al_2O_3$, Ag, $SiO_2$, *etc.*) to enable CMOS-compatible scale-up.[40,45,46]

### 2.2 Structure and parameters of the PtMM absorbers

We investigate two metal–insulator–metal (MIM) photonic metamaterial absorbers: a nanocross photonic metamaterial (NC-PtMM) and a nanosquare PtMM (NS-PtMM). The designs comprise a patterned top metal resonator, an $Al_2O_3$ dielectric spacer, and a multilayer reflective ground stack (Al/$SiO_2$/Ag). The unit-cell geometry is defined by the period $p$, resonator dimensions ($L$, $w$ for nanocrosses; $a$ for nanosquares), and the edge-to-edge gap $g$. The unit-cell geometries of NC-PtMM and NS-PtMM are illustrated in Fig. 1 and 2, respectively, and summarized in Table 1.

The corresponding layer stacks (materials and thicknesses) used in all simulations are listed in Table 2. Unless otherwise stated, the Ag ground plane is optically thick ($t_{Ag} \geq 100$ nm), so transmission is negligible ($T \approx 0$), and absorptance is determined primarily by suppression of reflectance *via* impedance

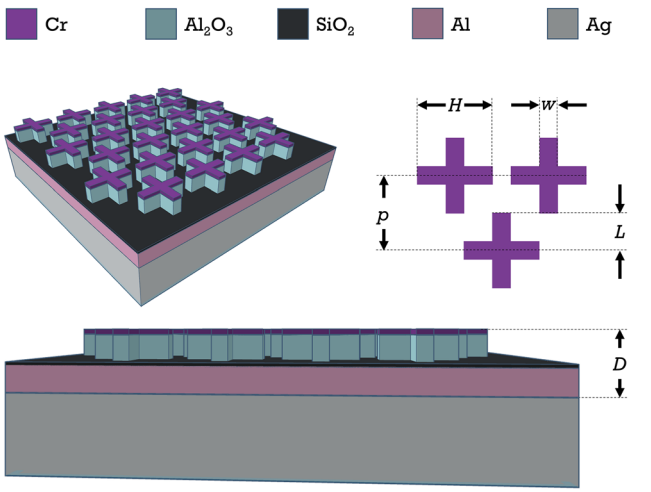


Fig. 1 Proposed nanocross photonic metamaterial (NC-PtMM) nanostructure for increasing the thermal gradient across TEGs. Nanocross structure consists of an ultra-thin Cr layer over an $Al_2O_3$ spacer. Ground plane consists of Al, $SiO_2$, and Ag. Unit-cell geometry and material stack are described in Tables 1 and 2, respectively.

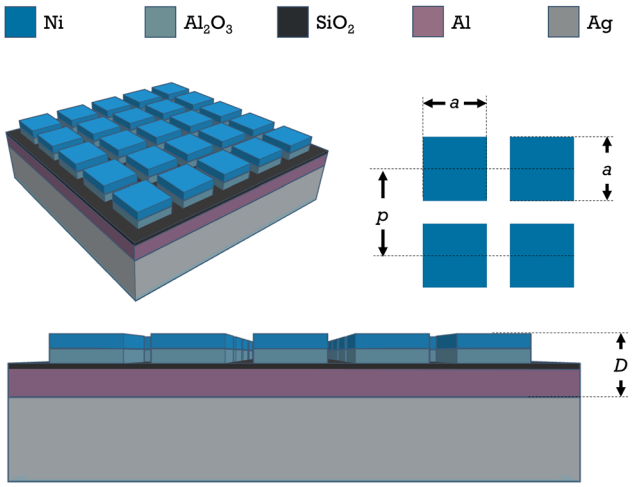


Fig. 2 Proposed nanosquare photonic metamaterial (NS-PtMM) nanostructure for increasing the thermal gradient across TEGs. The NS structure consists of an ultra-thin Ni layer over an $Al_2O_3$ spacer. Ground plane consists of Al, $SiO_2$, and Ag. Unit-cell geometry and material stack are described in Tables 1 and 2, respectively.

matching and resonant dissipation in the top resonator/spacer region.

While NC-PtMM attains superior peak and broadband absorptance, the simpler square/tiled resonator NS-PtMM is expected to provide a distinct set of practical benefits for (i) technology translation, (ii) scale-up, and (iii) Space qualification.[33,42,47–51] The square geometry reduces lithographic and process complexity: features are straight-edged and orthogonal (no multi-directional nanofabrication tolerances), single critical dimension control is sufficient to tune resonance position, and unit-cell symmetry permits the use of higher-throughput patterning approaches (photolithography, nanoimprint, interference lithography, and template methods) with relaxed resolution requirements. These attributes translate into higher fabrication yield, lower mask cost, and improved uniformity across large-area substrates. From a device reliability perspective, the square array produces a more spatially uniform absorptance and heating profile (fewer concentrated electromagnetic hot-spots), reducing local thermal stresses that can accelerate material degradation under thermal cycling and radiation exposure in Space.[52,53] Therefore, although NS-PtMM is less efficient in absolute absorptance per unit area, it is expected to provide manufacturability, robustness, and reduced sensitivity to dimensional error for large-area, low-cost, or flight-ready implementations where repeatability, qualification risk, and cost are primary concerns. Conceptual comparison between high-efficiency PtMM and high-deployability NS-PtMM is presented in Table S1.

Having defined the unit-cell geometry, quantities, and materials reported in this work (Fig. 1, 2 and Tables 1, 2), we next describe the numerical workflow used to obtain the optical response and the coupled photothermal dynamics.

### 2.3 Optical absorptance and impedance matching

The spectral absorptance is defined as

$$A(\lambda) = 1 - R(\lambda) - T(\lambda),$$

where $R(\lambda)$ and $T(\lambda)$ are reflectance and transmittance under plane-wave illumination. With an optically thick Ag ground plane ($t_{Ag} \geq 100$ nm; Table 2), transmission is negligible ($T \approx 0$) and $A(\lambda) = 1 - R(\lambda)$. Where layer-resolved absorption is discussed, we report the fractional absorbed power in each layer obtained from the volumetric loss density in the electromagnetic simulation. Near-unity absorptance $A(\lambda)$ is achieved by designing the metasurface impedance $Z_{PMA}$ to match free space impedance $Z_0$, minimising reflection:

$$R(\lambda) = \left|\frac{Z_{PMA}(\lambda) - Z_0}{Z_{PMA}(\lambda) + Z_0}\right|^2.$$

Fabry–Pérot resonance condition (dielectric spacer)

$$\delta = \frac{2\pi n d \cos\theta_t}{\lambda}, \text{ resonance for } \delta = m\pi.$$

### 2.4 Joule heating and transient thermal response

The electromagnetic solver yields the volumetric absorbed power density $Q(r, \lambda)$ [W m$^{-3}$], which is used as the heat source term in the time-dependent heat-transfer model:

$$Q(r,\lambda) = \frac{1}{2}\Re\{J(r,\lambda) \times E^*(r,\lambda)\} \approx \frac{1}{2}\sigma(\lambda)|E(r,\lambda)|^2,$$

which is used as the heat-source term in the time-dependent heat equation

$$\rho c_p \frac{\partial T}{\partial t} = \nabla \cdot (k\nabla T) + Q(r,t),$$

with $Q(r, t)$ obtained by spectrally weighting $Q(r, \lambda)$ with AM0 irradiance and applying temporal envelopes corresponding to the illumination scenario (steady or pulsed). See Methods/SI for details.

Table 1 Unit-cell geometry (NC-PtMM and NS-PtMM)

| Parameter | Symbol | NC-PtMM (Nanocross) | NS-PtMM (Nanosquare) |
|---|---|---|---|
| Period (pitch) | $p$ | 360 nm | 400 nm |
| Cross span (tip-to-tip) | $H$ | 300 nm | — |
| Cross arm half-length (centre-to-tip) | $L$ | 150 nm (= $H/2$) | — |
| Cross arm width | $w$ | 60 nm | — |
| Square side length | $a$ | — | 250 nm |
| Gap (edge-to-edge) | $g$ | 60 nm (= $p - H$) | 150 nm (= $p - a$) |
| Total stack thickness excluding bottom Ag | $D$ | 230 nm | 230 nm |

Table 2 Material stack and thicknesses

| | NC-PtMM (Nanocross) | | NS-PtMM (Nanosquare) | |
|---|---|---|---|---|
| Layer (top to bottom) | Material | Thickness | Material | Thickness |
| Patterned resonator | Cr | $t_m$ = 20 nm | Ni | $t_m$ = 20 nm |
| Primary spacer | $Al_2O_3$ | $s$ = 100 nm | $Al_2O_3$ | $s$ = 100 nm |
| Ground sublayer 1 | Al | $t_{Al}$ = 10 nm | Al | $t_{Al}$ = 10 nm |
| Ground sublayer 2 | $SiO_2$ | $t_{SiO2}$ = 100 nm | $SiO_2$ | $t_{SiO2}$ = 100 nm |
| Ground plane (optically thick) | Ag | $t_{Ag} \geq$ 100 nm | Ag | $t_{Ag} \geq$ 100 nm |
| Total thickness (excluding Ag) | — | $D$ = 230 nm | — | $D$ = 230 nm |

### 2.5 Materials, manufacturability, and Space-compatibility

The metamaterial designs presented deliberately use materials and thicknesses compatible with standard micro-/nano-fabrication sequences and with aerospace surface-coating practice.[16,18] Top resonators were chosen from commonly used thin-film metals (Cr, Ni, Al, Ag), while the dielectric spacer materials are standard oxides ($Al_2O_3$, $SiO_2$) available *via* atomic layer deposition (ALD) or sputtering. These choices enable the use of industry-standard processes (e-beam or nanoimprint lithography, thermal evaporation or sputter deposition, lift-off, and templated deposition such as AAO masks) and simplify scale-up and qualification. The selection also aligns with Space-material practice: Al and its oxide, Cr, Ni, and Ag are well documented in spacecraft hardware (structural and optical coatings), and the space environment concerns (thermal cycling, UV/radiation, atomic oxygen) can be addressed through coating thickness control, passivation, and standard testing protocols. Using these common materials reduces integration risk relative to exotic chemistries and accelerates the pathway to flight qualification.[54]

Fig. 3 shows the proof-of-patternability (geometry feasibility) of the NC-PtMM geometry with e-beam lithography at IIT. A standard PMMA resist, thin Al anti-charging layer, e-beam dose, and lift-off plus Ti/Au evaporation produced ~10 000 element arrays (full process described in SI). This is a mere demonstration of process feasibility using existing micro- and nano-fabrication resources.

Space-qualification screening should include high-flux UV/VUV exposure and proton/electron irradiation (TID and displacement damage) to assess photochemical and radiation-induced optical drift, ion-bombardment sputter/erosion testing to evaluate material loss, and mechanical vibration/shock per established NASA/ECSS environmental verification standards.[55–59] We select Cr with ALD $Al_2O_3$ passivation because Cr provides broadband optical loss in the visible, while $Al_2O_3$ is a well-established Space-relevant barrier against AO/VUV-induced degradation and is deposited by industry-standard ALD.[33,58,60–62]

The e-beam demonstrator (Ti/Au on $CaF_2$) is presented solely to confirm pattern fidelity and large-area manufacturability of the nanocross geometry; it is not an optical validation of the Cr-top NC-PtMM. Ti is used only as a standard adhesion layer for Au, while the optical design is optimized for Cr due to its stronger broadband loss in the visible. Importantly, our parametric comparison (Fig. 7b) shows that Cr-top resonators outperform Au-top resonators across the visible band relevant to AM0, indicating that the demonstrator material choice is conservative with respect to broadband solar absorption. In future work, the same fabrication route will be repeated using Cr (and optional ALD $Al_2O_3$ capping) and validated *via* measured $R/T/A$ spectra and thermal response under controlled illumination.

Practical considerations for Space deployment:

- AM0 spectral energy: the top-of-atmosphere solar constant $\approx$1361 W m$^{-2}$ with most energy in 400–2400 nm; PtMM design should therefore prioritise broad visible and NIR capture for maximum available power.[43]
- Thermal cycling and stability: thin metallic resonators must survive thermal cycling and radiation. Chromium and aluminium oxide are relatively robust; further radiation endurance testing is recommended.
- Integration: PtMMs can be implemented as a top coating on the hot side of standard TEG devices (no change to the TE legs required). Thermal interface engineering (adhesives, micro-contacts) must prioritise high conductance from the resonator layer into the TE hot plate while maintaining thermal isolation to the cold sink.
- Power estimates: converting $\Delta T$ to electrical power requires module-level modelling ($ZT$, contact resistances, leg geometry). We recommend follow-on finite-element electrothermal models that include the full TE module to quantify expected mW–W gains per unit area.

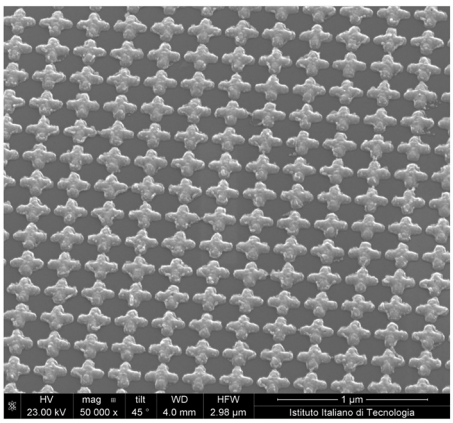


Fig. 3 NC-PtMM-like geometry. NC dimensions are comparable to NC-PtMM, as is the inter-NC distance.

## 3. Results and discussion

### 3.1 Optical performance of proposed PtMMs

Unless explicitly varied in parametric sweeps, all simulations use the unit-cell parameters given in Fig. 1, 2 and Table 1.

Fig. 4 and 5 report the complete optical balance – reflectance $R(\lambda)$, transmittance $T(\lambda)$, and the derived absorptance $A(\lambda) = 1 - R(\lambda) - T(\lambda)$ – for the two optimized metasurfaces. The NC-PtMM (Fig. 4a and b) attains near-unity absorptance in the visible: the simulated peak absorptance reaches $\approx$99%, and the visible-band average is $\approx$95% (range reported over 300–700 nm unless otherwise stated). The high absorptance arises from the hybridized response of localized plasmonic resonances in the nanocross and the Fabry–Pérot-like cavity formed by the dielectric spacer and the reflective ground plane; the overlap of several resonant channels produces a low-$Q$, broadband profile that matches the AM0 visible photon flux. By contrast, the NS-PtMM (nanosquares, Fig. 4c and d) demonstrates a broader but shallower response (visible-average $\approx$ 68–78%). The square tiles support fewer overlapping localised modes and therefore present larger residual reflection in spectral sub-bands; however, their reduced $Q$ and simpler geometry provide greater fabrication tolerance (see SI). NS-PtMM is included as a manufacturability-motivated reference design; additional NS optimisation is left for future work. For completeness, we also plot the absorptance contributions in layer-resolved form (top resonator, spacer, ground). For NC-PtMM, most of the dissipated optical power localises at the top metal/spacer interface and in the top resonator, indicating efficient conversion of photon energy into local Joule heating suitable for fast surface temperature rise. The NC design exhibits strong, surface-localised absorptance, making it ideal for raising the TEG hot-side temperature with minimal added mass; the NS design trades peak absorptance for manufacturability and a more uniform heating footprint, reducing thermal stress. For device-level projections, we therefore evaluate NC-PtMM peak-power in the following section, and discuss NS-PtMM system robustness (in SI).

**3.1.1 Mechanism of photothermal gradient formation.** Fig. 5 links the electromagnetic absorption process to the resulting thermal localisation. The near-field maps at the vacuum/Cr and Cr/$Al_2O_3$ interfaces (Fig. 5a and b) show strong field confinement at nanocross edges and the resonator-spacer boundary, consistent with resonant dissipation in the lossy Cr layer and impedance-matching behaviour of the MIM absorber. The absorbed power density $Q(r)$ shown in Fig. 5c confirms that optical energy is predominantly converted to heat within the resonator/spacer region rather than deep in the substrate. The corresponding steady/quasi-steady temperature field (Fig. 5d) demonstrates spatial localisation of heating on the hot side, providing the physical basis for an increased temperature differential available to a thermoelectric module. Transient ns-pulse excitation is treated separately in Fig. 7 to quantify the peak non-equilibrium $\Delta T_{max}$ and characteristic thermal time scales. For an optically thick ground plane ($T \approx 0$), the

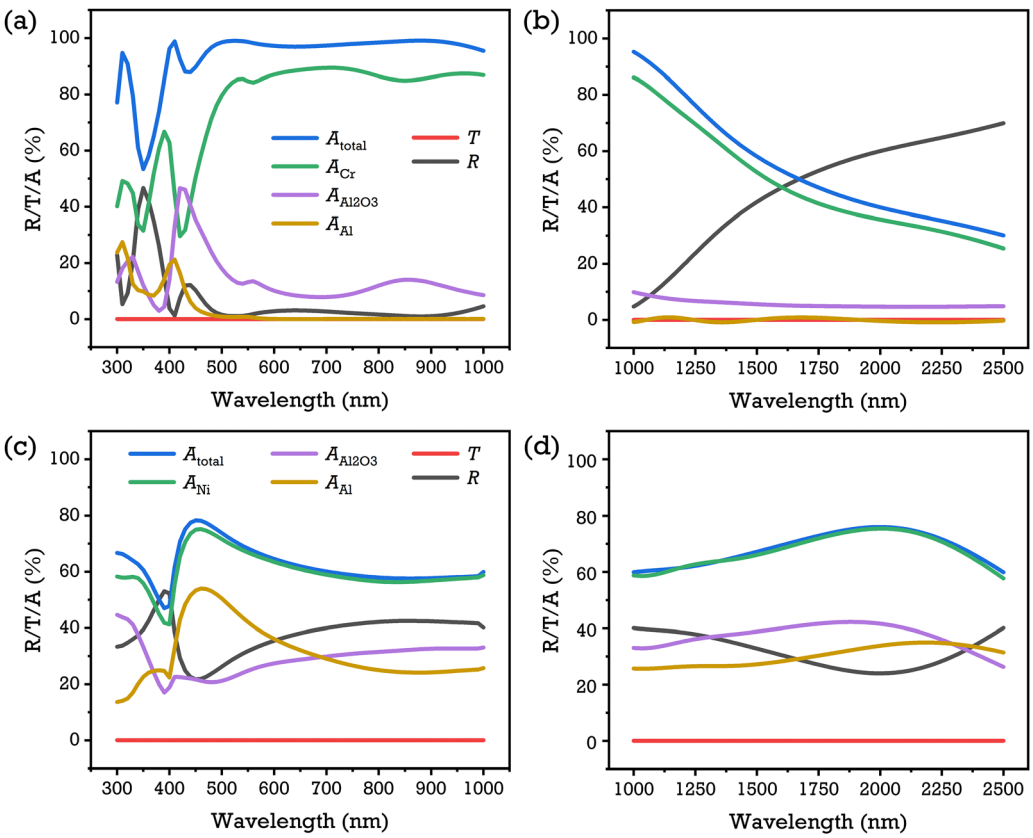


Fig. 4 Reflectance (black), transmittance (red), and absorptance (blue, green, magenta, and gold for total, top resonator, spacer, ground, respectively) of NC-PtMM and NS-PtMM in visible and NIR ranges. (a) and (b) NC-PtMM in the visible and NIR spectrum. (c) and (d) NS-PtMM in the visible and NIR spectrum.

 

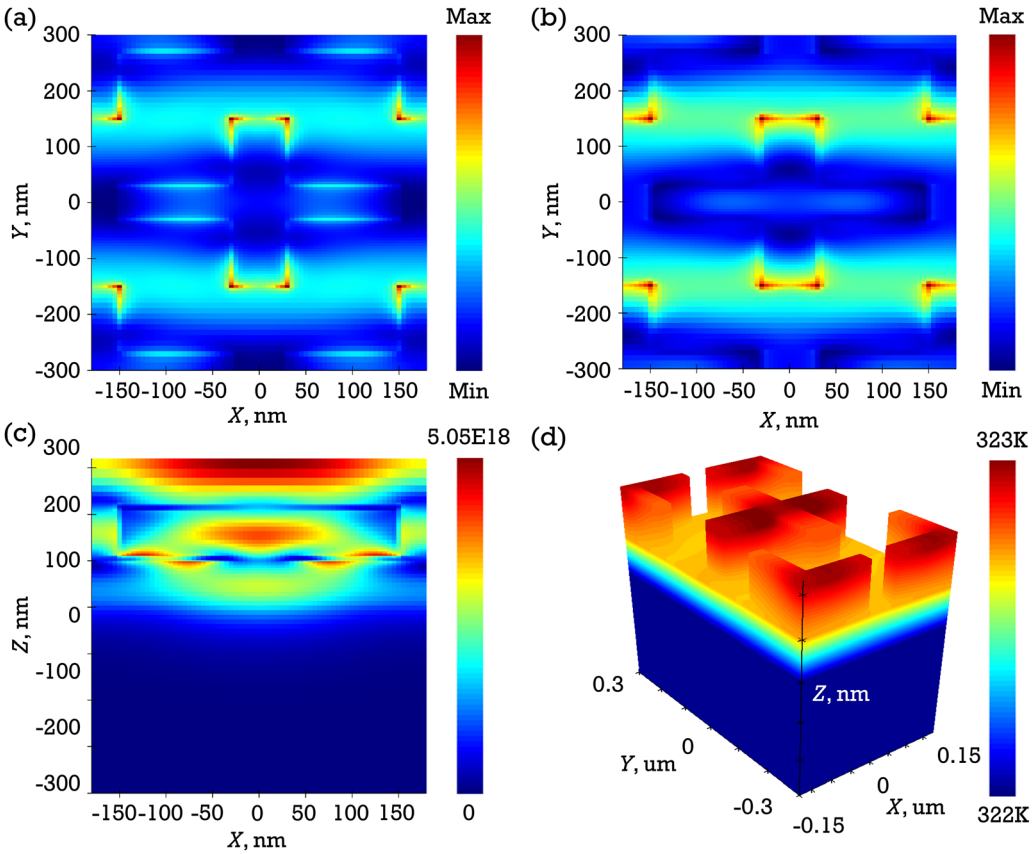


Fig. 5 Electromagnetic-to-thermal conversion mechanism in the NC-PtMM. (a) Normalised electric-field intensity $|E|^2/|E_0|^2$ at the vacuum/Cr interface and (b) at the Cr/$Al_2O_3$ interface, showing strong near-field localisation at nanocross edges and the resonator–spacer boundary. (c) Cross-sectional absorbed power density $Q(r)$ (resistive loss density, W $m^{-3}$), highlighting where optical energy is dissipated within the resonator/spacer region. (d) Steady (quasi-steady) temperature localisation $T(r)$ under continuous irradiation for the 20 nm-Cr design, illustrating that the temperature rise is concentrated near the same region where $Q(r)$ is maximal. The ns-pulse transient $\Delta T_{max}$ and its dependence on pulse width are quantified separately in Fig. 7.

near-unity absorptance corresponds to suppression of reflectance *via* effective impedance matching ($Z \approx Z_0$) and resonant dissipation in the lossy resonator/spacer region.

Fig. 6 summarises parametric sweeps that define the NC-PtMM process window. Panel (a) shows the effect of top-resonator (Cr) thickness on total absorptance: as thickness increases from thin-film limits up to ~35–60 nm, the structure transitions from under-coupled to optimally lossy, producing a broad absorptance plateau; beyond an optimum value, the spectral weight shifts to longer wavelengths and integrated visible absorptance declines. Panel (b) demonstrates the high sensitivity to spacer thickness ($Al_2O_3$): the spacer controls the effective cavity phase. It therefore tunes the spectral overlap between resonant channels – a ~±10–20 nm change produces measurable spectral shifts. Panels (c) and (d) show secondary sensitivity to the Al reflector thickness and the auxiliary $SiO_2$ spacer: both parameters have weaker influences provided a continuous reflective ground plane is present, but they afford a secondary tuning knob to suppress residual reflectance in the NIR tail. From the maps, we extract a practical process window: Cr thickness near 20 nm and $Al_2O_3$ spacer near 100 nm produce near-optimal visible absorptance while leaving a moderate margin for deposition variation. These maps are the basis for the fabrication recipe and for the robustness metrics reported in the SI.

Fig. 7a shows the effect of cross-arm width $w$ on spectral absorptance, which tunes near-field confinement and inter-element capacitive coupling. Here, an optimum width of ~60 nm yields maximal visible integrated absorptance while wider arms push the resonant features toward red/near-IR regions. Notably, $w$ is a second-order knob relative to resonator thickness $d_{Cr}$ (see Fig. 5a), but is important for fine bandwidth control and for suppressing side-lobe reflectance in the NIR-II range. Fig. 7b compares Cr and Au as top-metal resonators. Chromium's relatively large imaginary permittivity in the visible yields stronger, broader absorptance than Au for these MIM geometries – this is well illustrated by the nearly 3–4-fold increase in absorptance in specific spectral windows when substituting Cr for Au in our parametric runs. The Cr choice, therefore, represents an optimal trade-off between broadband absorptance, stability, and compatibility with thin-film processing.

Key optical optimisation observations: (i) Cr is crucial as resonator material in the intended wavelength band due to higher imaginary permittivity and broader coupling; (ii) resonator thickness and spacer thickness are primary tuning knobs

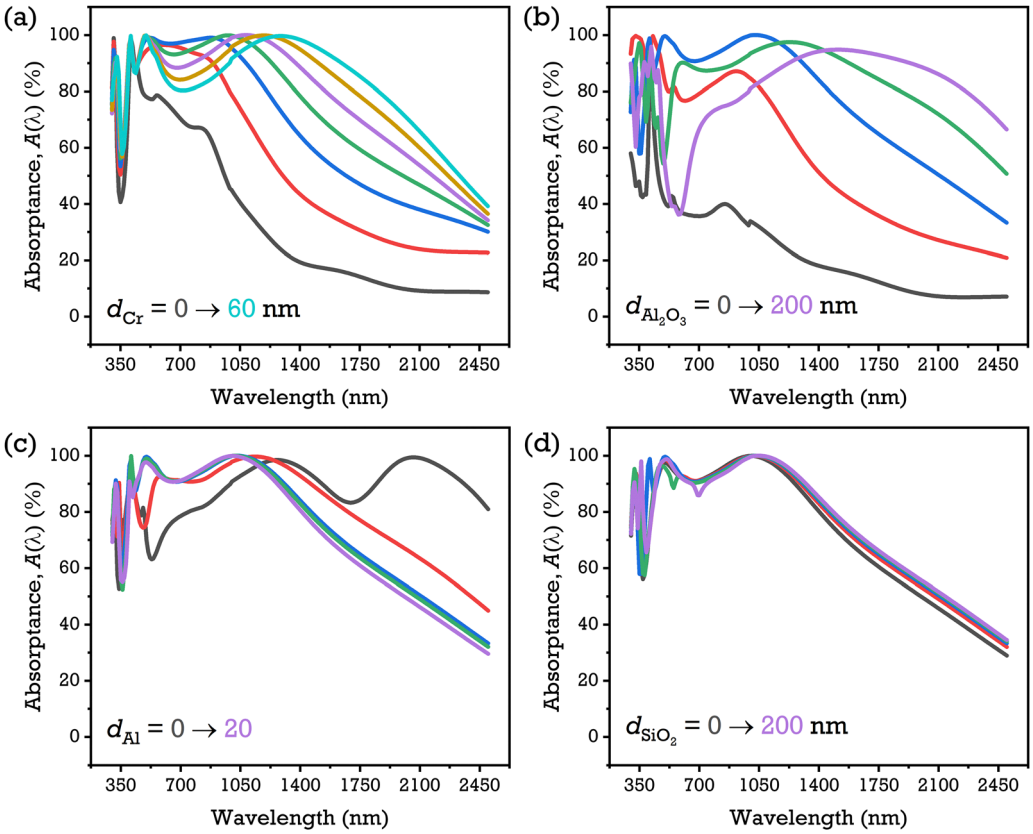


Fig. 6 Thickness optimisation map of NC-PtMM nanostructure. (a) Cr resonator thickness *vs.* absorptance: 0, 10, 20, 30, 40, 50, and 60 nm correspond to dark grey, red, blue, green, lavender, amber, and turquoise curves, respectively. (b) $Al_2O_3$ spacer thickness *vs.* absorptance: 0, 50, 100, 150, and 200 nm correspond to dark grey, red, blue, green, and lavender curves, respectively. (c) Al reflector thickness effect: 0, 5, 10, 15, and 20 nm correspond to dark grey, red, blue, green, and lavender curves, respectively. (d) $SiO_2$ spacer thickness effect: 0, 50, 100, 150, and 200 nm correspond to dark grey, red, blue, green, and lavender curves, respectively.

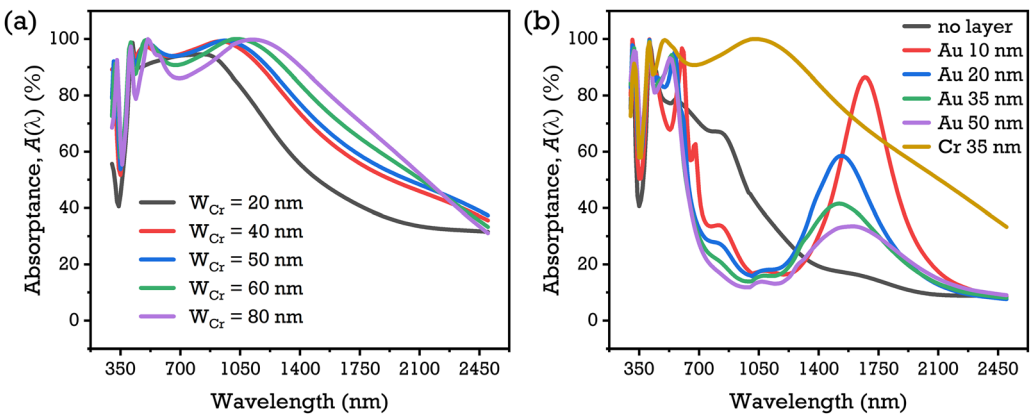


Fig. 7 NC width optimisation and top resonator materials comparison of NC-PtMM nanostructure: (a) NC width *vs.* absorptance, (b) Cr *versus* Au resonator comparison.

for absorptance magnitude and spectral position. Width and height are secondary but useful for bandwidth fine-tuning.

Fig. 8a quantifies the dependence of peak temperature difference ($\Delta T_{max}$) between the Cr top surface and the Ag substrate bottom on pulse width for the selected pulse train (1–20 ns). The results show a strong, non-linear dependence: short pulses (1 ns) produce modest $\Delta T_{max}$ ($\sim$17 K), while longer pulses (20 ns) produce transient $\Delta T$ in excess of 100 K, peaking at $\approx$117–155 K for the first and second pulses, respectively, in the reported run. This trend follows simple thermal physics: for

 

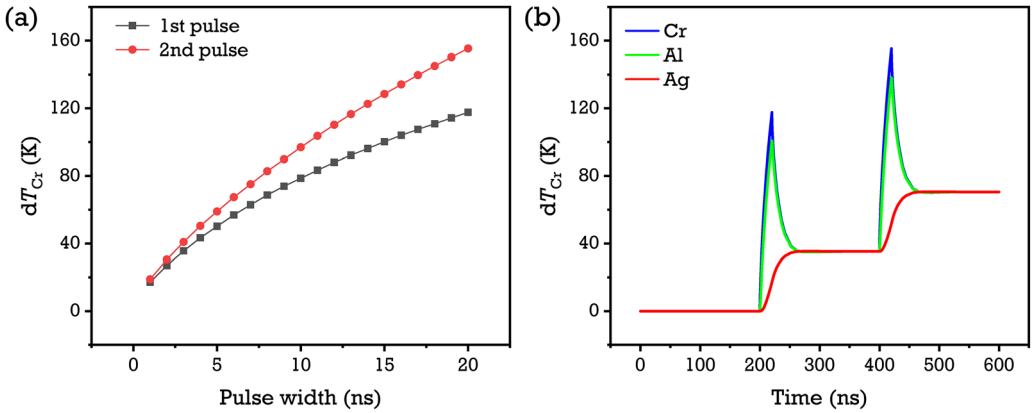


Fig. 8 (a) Dependence of the $\Delta T_{max}$, calculated between the Cr surface and the Ag substrate, on the pulse width in the range from 1 to 20 ns. (b) $\Delta T_{max}$ between the Cr, Al, and Ag surfaces, respectively, and the bottom of the Ag substrate, when the pulse width is equal to 20 ns.

a fixed pulse fluence, longer pulses deliver more energy into the metal volume before heat can diffuse away, thereby increasing the peak temperature. Additionally, pulse trains lead to residual heating accumulation between pulses (especially in the substrate), which augments $\Delta T$ for subsequent pulses. Fig. 7b, in turn, shows layer-resolved $\Delta T$ for a 20 ns pulse: the maximum transient temperature difference is observed between the Cr nanocross top surface and the Ag substrate bottom. At the same time, intermediate regions—specifically the dielectric spacer ($Al_2O_3$) and any thin interlayers—exhibit smaller amplitude responses and faster thermal relaxation. The Ag substrate's larger thermal mass sustains the residual temperature difference for longer timescales relevant to thermoelectric harvesting. Practically, these coupled dynamics indicate the PtMM can create short-lived but large $\Delta T$ transients that a TEG hot contact can sample – design of the thermal interface (high conductance to the TE hot plate, thermal isolation from the cold sink) is therefore critical to convert $\Delta T$ into usable electrical power. Short (ns-scale) pulses were used in the transient simulations as a numerical probe to reveal the intrinsic non-equilibrium photothermal response of the metasurface – in particular, the maximum instantaneous temperature rise and the time-scales on which optical absorptance is converted into local Joule heating before lateral and bulk heat diffusion act. These pulses emulate (a) laboratory pulsed-laser interrogation commonly used to characterise photothermal transients and (b) extreme, temporally localised concentrated illumination events.

The ns-pulse results above quantify the intrinsic transient response and peak non-equilibrium $\Delta T_{max}$, but continuous AM0 illumination is steady. In steady operation, the temperature rise is governed by the balance of absorbed areal power $Q_{abs}$ and the effective thermal resistance $R_{th}$ between the heated region and the cold sink, $\Delta T \approx Q_{abs} \times R_{th}$. For a broadband absorber $Q_{abs} \approx A_{eff} \times I_{AM0}$ (or $C \times A_{eff} \times I_{AM0}$ under optical concentration factor $C$). Table S3 (SI) provides representative $\Delta T$ values *versus* $R_{th}$ and $C$, showing that tens of kelvin steady $\Delta T$ requires optical concentration and/or deliberate thermal isolation, while the PtMM increases $Q_{abs}$ and thus reduces the concentration/isolation required for a given target $\Delta T$.

### 3.2 Temperature gradient $\Delta T$

We coupled full Maxwell simulations with time-dependent heat transfer (COMSOL Multiphysics) to evaluate transient heating under pulsed AM0-like illumination (train of pulses, $P_{width}$ = 20 ns, $P_{period}$ = 200 ns as a probing scheme). NC-PtMM exhibits extremely strong local heating: $\Delta T_{max}$ between the Cr nanocross top surface and the Ag substrate bottom surface reached 117.7 K (first pulse) and 155.3 K (second pulse) under the specified pulsed excitation. Shorter pulses produce smaller $\Delta T_{max}$, but the trend indicates strong dependence on pulse width and local heat capacity/thermal conductance. Importantly, the Ag substrate maintains a more persistent gradient than the thin top films, which is advantageous for conduction into a thermoelectric leg.

**3.2.1 Interpretation for TEG harvesting.** The plasmonically-generated hot-spot provides a strong local $\Delta T$ that, with proper coupling to the hot side of a thermoelectric leg and a well-engineered cold sink, can translate into larger open-circuit voltages and power density than an identical TEG with a bare (non-metamaterial) absorber. These results align with earlier theoretical studies that demonstrated the potential of MPAs to intensify thermal gradients in TE devices.[23]

### 3.3 Generated electrical power estimation

To translate temperature differentials into expected electrical power,[63] we use a representative commercial $Bi_2Te_3$ thermoelectric module (127 thermocouple pairs; module datasheet used for parameters).[64,65] Typical device parameters are Seebeck per couple $S_{pair} \approx 200$ μV $K^{-1}$ ($Bi_2Te_3$ at room temperature), number of couples $N = 127$, and a typical module internal resistance $R_{int} = 4$ Ω. The module Seebeck is therefore $S_{tot} = N \times S_{pair} \approx 0.0254$ V $K^{-1}$. The open circuit voltage is $V_{oc} = S_{tot}\Delta T$, and the maximum extractable power into a matched load is $P_{max} = V_{oc}^2/(4R_{int}) = S_{tot}^2\Delta T/(4R_{int})$. Table 3 summarises representative outputs for common $\Delta T$ values.

Table 3 emphasises two critical points for system design: (i) electrical power scales as $\Delta T^2$, so the transient high $\Delta T$ achievable in non-equilibrium pulses (50–100 K) rapidly

Table 3 Representative TE module outputs (30 × 30 $mm^2$ module)

| $\Delta T$ (K) | $V_{oc}$ (V) | $P_{max}$ (W) | $P_{max}$ per $cm^2$ |
|---|---|---|---|
| 1 | 0.0254 | $4.03 \times 10^{-5}$ | 4.48 μW $cm^{-2}$ |
| 10 | 0.254 | $4.03 \times 10^{-3}$ | 0.448 mW $cm^{-2}$ |
| 50 | 1.27 | $1.01 \times 10^{-1}$ | 11.2 mW $cm^{-2}$ |
| 100 | 2.54 | $4.03 \times 10^{-1}$ | 44.7 mW $cm^{-2}$ |

increases output, and (ii) steady-state unconcentrated AM0 without thermal isolation yields $\Delta T \ll 10$ K, so mission design must incorporate optical concentration or thermal design to exploit the PtMM advantage in continuous operation.

### 3.4 Limitations and next steps

The present study is primarily numerical and focuses on establishing design rules and mechanisms for PtMM-enhanced photothermal gradients. The e-beam fabrication shown (Ti/Au) serves as a proof-of-patternability for the NC-PtMM geometry and does not constitute an optical/thermal validation of the Cr-stack design. The next experimental step is therefore to fabricate the $Cr/Al_2O_3/Al/SiO_2/Ag$ stack (with optional ALD $Al_2O_3$ capping), measure $R(\lambda)$, $T(\lambda)$, and $A(\lambda)$ under a calibrated illumination source, and compare the measured absorptance with the simulated spectra. Thermal validation will then be performed by measuring the hot-side temperature rise and the top-bottom $\Delta T$ under controlled continuous illumination and under pulsed-laser probing, followed by module-level tests using a commercial $Bi_2Te_3$ device to quantify $V_{oc}$ and output power. These experiments will also clarify the role of optical concentration and thermal-interface engineering in achieving steady AM0-relevant $\Delta T$ gains.

## 4. Conclusion

We designed two industry-compatible metal–insulator–metal (MIM) photonic metamaterial absorbers intended to augment thermoelectric generators (TEGs) in Space environments by increasing the usable temperature differential at the hot side: a nanocross PtMM (NC-PtMM) and a nanosquare PtMM (NS-PtMM), both based on thin-film stacks using common microfabrication materials (Cr/Ni, $Al_2O_3$, Al, $SiO_2$, and an optically thick Ag ground plane). Full-wave simulations show that the NC-PtMM design achieves near-unity visible absorptance and strongly suppressed reflectance with negligible transmission due to the thick ground plane. The NS-PtMM design exhibits lower absorptance but provides a manufacturability-motivated reference geometry; further NS-PtMM optimisation is beyond the scope of the present work. Interface-resolved $|E|^2$ maps, volumetric resistive loss density $Q(r)$, and steady temperature localisation collectively demonstrate that absorption is concentrated in the resonator/spacer region, consistent with impedance-matching behaviour of MIM absorbers and resonant dissipation in the lossy top metal. Using ns-scale pulsed illumination as a transient probe, we quantified the intrinsic non-equilibrium photothermal response and the peak $\Delta T_{max}$ achievable on short time scales; these transients establish the upper bound of instantaneous temperature gradients that can be presented to a TEG hot contact under temporally localised excitation. A worked example based on representative $Bi_2Te_3$ module parameters translates $\Delta T$ into expected $V_{oc}$ and $P_{max}$, illustrating the strong quadratic scaling of deliverable power with $\Delta T$ and motivating optical concentration and thermal-interface engineering for steady operation. The Ti/Au e-beam demonstrator is presented as proof-of-patternability of the nanocross geometry; it is not an optical validation of the Cr-top stack. Our Cr-*vs.*-Au comparison shows that Cr is preferred for broadband AM0-relevant absorption. Next steps are fabrication of the $Cr/Al_2O_3/Al/SiO_2/Ag$ stack (with optional ALD oxide capping), experimental measurement of $R/T/A$ spectra and temperature rise under calibrated continuous and pulsed illumination, and module-level demonstration with commercial TEGs, including Space-qualification screening (AO, TVAC, UV/VUV and radiation).

## 5. Experimental/methods

### 5.1 Optical and thermal simulations

Full-wave electromagnetic simulations coupled with time-dependent heat transfer were performed in COMSOL Multiphysics (version used in the project). The electromagnetic model used measured/standard optical constants for Cr, Al, Ag, Ni, $Al_2O_3$, and $SiO_2$.[66,67] Illumination was treated as normal incidence AM0 spectral content integrated to $\approx$1361 W $m^{-2}$ on an optimised structure for the wavelength bands evaluated (300–2500 nm). Transient heating used a pulsed illumination train ($P_{width}$ and $P_{period}$ as reported) to probe fast heating and relaxation dynamics. Specific solver settings, mesh, and boundary conditions are detailed in SI.

## Conflicts of interest

There are no conflicts to declare.

## Data availability

All data supporting the conclusions of this manuscript are provided in the article and in the supplementary information (SI), which includes additional manufacturability and process-window analysis (Table S1), a condensed Space-qualification test matrix (Table S2), fabrication-feasibility and Nanoscribe route details, a coupled electromagnetic/thermal simulation recipe, steady-state $\Delta T$ scaling calculations (Table S3), and polarisation-dependent absorptance data (Fig. S1). See DOI: https://doi.org/10.1039/d5cp04738b.

## Acknowledgements

We acknowledge the RGC HK grant (HKBU 22300324) and the startup funding from Hong Kong Baptist University. We acknowledge the European Space Agency (ESA) Discovery & Preparation support and the Italian Institute of Technology nanofabrication facility for access to e-beam lithography used in this work. This work is dedicated to the memory of

 

Aliaksandr Hubarevich. His friendship, collaboration, and scientific rigour were an inspiration to us all. We also honour his wife, Volha, and son Paisij.



## References

1 D. M. Bushnell, R. W. Moses and S. H. Choi, Frontiers of Space Power and Energy NASA/TM-20210016143, 2021, https://ntrs.nasa.gov/citations/20210016143.
2 A. Datas and A. Martí, Thermophotovoltaic energy in space applications: review and future potential, *Solar Energy Materi. Solar Cells*, 2017, **161**, 285–296.
3 R. Verduci, V. Romano, G. Brunetti, N. Yaghoobi Nia, A. Di Carlo, G. D'Angelo and C. Ciminelli, Solar Energy in Space Applications: Review and Technology Perspectives, *Adv. Energy Mater.*, 2022, **12**, DOI: 10.1002/aenm.202200125.
4 1st Space Exploration Conference: Continuing the Voyage of Discovery, American Institute of Aeronautics and Astronautics, Reston, Virigina, 01302005.
5 C. E. Whiting and D. F. Woerner, in *The Technology of Discovery*, ed. D. F. Woerner, Wiley, 2023, pp. 183–212.
6 S. Antharam, M. I. Khan, L. Franke, Z. Wang, N. Luo, J. Feßler, W. Xie, U. Lemmer and M. M. Mallick, Milliwatt-scale 3D thermoelectric generators via additive screen printing, *Energy Environ. Sci.*, 2025, **18**, 7648–7659.
7 X. Zhao, W. Han, Y. Jiang, C. Zhao, X. Ji, F. Kong, W. Xu and X. Zhang, A honeycomb-like paper-based thermoelectric generator based on a $Bi_2Te_3$/bacterial cellulose nanofiber coating, *Nanoscale*, 2019, **11**, 17725–17735.
8 K. H. Spring, Generation of Electricity Without the use of Rotating Machinery, *Nature*, 1961, **190**, 297–299.
9 P. D. Dunn and J. K. Wright, Unconventional methods of electricity generation, *Proc. Inst. Electr. Eng.*, 1963, **110**, 1837.
10 G. B. Soares, J. J. G. Ledesma, E. A. Da Silva and O. H. Ando, Junior, Thermoelectric Generators Applied as a Power Source in CubeSats: State of the Art, *Energies*, 2025, **18**, 173.
11 M. M. Garzon, *Development and analysis of the thermal design for the OSIRIS-3U CubeSat*, 2012.
12 A. Ostrufka, E. M. Filho, A. C. Borba, A. W. Spengler, T. S. Possamai and K. V. Paiva, Experimental evaluation of thermoelectric generators for nanosatellites application, *Acta Astronaut.*, 2019, **162**, 32–40.
13 T. G. Novak, K. Kim and S. Jeon, 2D and 3D nanostructuring strategies for thermoelectric materials, *Nanoscale*, 2019, **11**, 19684–19699.
14 Y. Tian, G.-K. Ren, Z. Zhou, Z. Wei, W. Fang, J. Song, Y. Shi, X. Chen and Y.-H. Lin, Optimizing the output performance and parasitic depletion of $Bi_2Te_3$-based thermoelectric generators by using a high-density approach, *J. Mater. Chem. A*, 2023, **11**, 9464–9473.
15 G. J. Snyder and E. S. Toberer, Complex thermoelectric materials, *Nat. Mater.*, 2008, **7**, 105–114.
16 C. M. Watts, X. Liu and W. J. Padilla, Metamaterial electromagnetic wave absorbers, *Adv. Mater.*, 2012, **24**(OP98-120), OP181.
17 Y. Xiao, C. Ma, T. Sun, Q. Song, L. Bian, Z. Yi, Z. Hao, C. Tang, P. Wu and Q. Zeng, Investigation of a high-performance solar absorber and thermal emitter based on Ti and InAs, *J. Mater. Chem. A*, 2024, **12**, 29145–29151.
18 N. I. Landy, S. Sajuyigbe, J. J. Mock, D. R. Smith and W. J. Padilla, Perfect metamaterial absorber, *Phys. Rev. Lett.*, 2008, **100**, 207402.
19 A. Hubarevich, M. Marus, W. Fan, A. Smirnov and H. Wang, Highly Efficient Ultrathin Plasmonic Insulator–Metal–Insulator–Metal Solar Cell, *Plasmonics*, 2018, **13**, 141–145.
20 M. Marus, Y. Mukha, H.-T. Wong, T.-L. Chan, A. Smirnov, A. Hubarevich and H. Hu, Tsuchime-like Aluminum Film to Enhance Absorption in Ultra-Thin Photovoltaic Cells, *Nanomaterials*, 2023, **13**, DOI: 10.3390/nano13192650.
21 K. Aydin, V. E. Ferry, R. M. Briggs and H. A. Atwater, Broadband polarization-independent resonant light absorption using ultrathin plasmonic super absorbers, *Nat. Commun.*, 2011, **2**, 517.
22 M. Yan, Metal–insulator–metal light absorber: a continuous structure, *J. Opt.*, 2013, **15**, 25006.
23 S. Katsumata, T. Tanaka and W. Kubo, Metamaterial perfect absorber simulations for intensifying the thermal gradient across a thermoelectric device, *Opt. Express*, 2021, **29**, 16396–16405.
24 R. Nakayama, S. Saito, T. Tanaka and W. Kubo, Metasurface absorber enhanced thermoelectric conversion, *Nanophotonics*, 2024, **13**, 1361–1368.
25 J. Hao, L. Zhou and M. Qiu, Nearly total absorption of light and heat generation by plasmonic metamaterials, *Phys. Rev. B: Condens. Matter Mater. Phys.*, 2011, **83**, 165107.
26 Y. Pan, G. Tagliabue, H. Eghlidi, C. Höller, S. Dröscher, G. Hong and D. Poulikakos, A Rapid Response Thin-Film Plasmonic-Thermoelectric Light Detector, *Sci. Rep.*, 2016, **6**, 37564.
27 W. Kubo, M. Kondo and K. Miwa, Quantitative Analysis of the Plasmonic Photo-Thermoelectric Phenomenon, *J. Phys. Chem. C*, 2019, **123**, 21670–21675.
28 J. F. Serrano-Claumarchirant, C. Cho, A. Cantarero, M. Culebras, R. Abargues and C. M. Gómez, How Plasmon Ag Nanoparticles can Enhance the Power Performance of a Thermoelectric Generator, *Small*, 2024, **20**, e2400345.
29 R. K. Kashyap and P. P. Pillai, Plasmonic Nanoparticles Boost Solar-to-Electricity Generation at Ambient Conditions, *Nano Lett.*, 2024, **24**, 5585–5592.
30 J. Bai, Z. Pang, P. Shen, T. Chen, W. Shen, S. Wang and S. Chang, A terahertz photo-thermoelectric detector based on metamaterial absorber, *Opt. Commun.*, 2021, **497**, 127184.
31 W. Kubo, in Proceedings of the 2022 Conference on Lasers and Electro-Optics Pacific Rim, Optica Publishing Group, Washington, DC, CTuP16E_02.
32 K. K. de Groh, B. A. Banks, S. K. Miller and J. A. Dever, *Handbook of Environmental Degradation of Materials*, Elsevier, 2018, pp. 601–645.
33 K. K. de Groh and B. A. Banks, Atomic Oxygen Erosion Data from the MISSE 2-8 Missions NASA/TM—2019-219982, 2019, https://ntrs.nasa.gov/citations/20190025445.

34 R. S. Soler Chisabas, D. F. Cantor, G. Loureiro and C. D. O. Lino, Method for CubeSat Thermal-Vacuum Cycling Test Specification, 47th International Conference on Environmental Systems, 2017.
35 P. Giordano, New Testing Standard For European Programs, *Environ. Testing Space Prog.*, 2004, **558**, 385–392.
36 ISO 24412:2023(en), Space systems—Thermal vacuum environmental testing, https://www.iso.org/obp/ui/en/#iso:std:iso:24412:ed-1:v1:en, (accessed 19 November 2025).
37 R. Cooper, H. P. Upadhyaya, T. K. Minton, M. R. Berman, X. Du and S. M. George, Protection of polymer from atomic-oxygen erosion using $Al_2O_3$ atomic layer deposition coatings, *Thin Solid Films*, 2008, **516**, 4036–4039.
38 K. Bhattarai, S. Silva, K. Song, A. Urbas, S. J. Lee, Z. Ku and J. Zhou, Metamaterial Perfect Absorber Analyzed by a Metacavity Model Consisting of Multilayer Metasurfaces, *Sci. Rep.*, 2017, **7**, 10569.
39 B.-X. Wang, C. Xu, G. Duan, W. Xu and F. Pi, Review of Broadband Metamaterial Absorbers: From Principles, Design Strategies, and Tunable Properties to Functional Applications, *Adv. Funct. Mater.*, 2023, **33**, DOI: 10.1002/adfm.202213818.
40 S. Ogawa and M. Kimata, Metal–Insulator–Metal-Based Plasmonic Metamaterial Absorbers at Visible and Infrared Wavelengths: A Review, *Materials*, 2018, **11**, DOI: 10.3390/ma11030458.
41 W. Ma, Y. Wen and X. Yu, Broadband metamaterial absorber at mid-infrared using multiplexed cross resonators, *Opt. Express*, 2013, **21**, 30724–30730.
42 H. Xiong, J.-S. Hong, C.-M. Luo and L.-L. Zhong, An ultrathin and broadband metamaterial absorber using multilayer structures, *J. Appl. Phys.*, 2013, **114**, DOI: 10.1063/1.4818318.
43 G. Thuillier, L. Floyd, T. N. Woods, R. Cebula, E. Hilsenrath, M. Hersé and D. Labs, in *Solar Variability and Its Effects on Climate*, ed. J. M. Pap, P. Fox, C. Frohlich, H. S. Hudson, J. Kuhn, J. McCormack, G. North, W. Sprigg and S. T. Wu, American Geophysical Union, Washington, DC, 2004, pp. 171–194.
44 T. N. Woods, P. C. Chamberlin, J. W. Harder, R. A. Hock, M. Snow, F. G. Eparvier, J. Fontenla, W. E. McClintock and E. C. Richard, Solar Irradiance Reference Spectra (SIRS) for the 2008 Whole Heliosphere Interval (WHI), *Geophys. Res. Lett.*, 2009, **36**, DOI: 10.1029/2008GL036373.
45 N. Mou, X. Liu, T. Wei, H. Dong, Q. He, L. Zhou, Y. Zhang, L. Zhang and S. Sun, Large-scale, low-cost, broadband and tunable perfect optical absorber based on phase-change material, *Nanoscale*, 2020, **12**, 5374–5379.
46 R. F. Wolffenbuttel and M. A. Ghaderi, Design of large-area metasurfaces for the mid-IR and suited for CMOS-compatible fabrication by masked lithography, *Photonics Nanostruct. Fundam. Appl.*, 2022, **51**, 101050.
47 A. de Rooij, in *Encyclopedia of Aerospace Engineering*, ed. R. Blockley and W. Shyy, Wiley, 2010.
48 B. A. Banks, S. K. Rutledge, J. A. Brady and J. E. Merrow, *Atomic oxygen effects on materials*, NASA, Langley Research Center, NASA(SDIO Space Environmental Effects on Materials Workshop, Part 1), 1989.
49 J. G. Ok, H. S. Youn, M. K. Kwak, K.-T. Lee, Y. J. Shin, L. J. Guo, A. Greenwald and Y. Liu, Continuous and scalable fabrication of flexible metamaterial films *via* roll-to-roll nanoimprint process for broadband plasmonic infrared filters, *Appl. Phys. Lett.*, 2012, **101**, DOI: 10.1063/1.4767995.
50 D. K. Oh, T. Lee, B. Ko, T. Badloe, J. G. Ok and J. Rho, Nanoimprint lithography for high-throughput fabrication of metasurfaces, *Front. Optoelectron.*, 2021, **14**, 229–251.
51 C. Wu, B. Neuner, III, G. Shvets, J. John, A. Milder, B. Zollars and S. Savoy, Large-area wide-angle spectrally selective plasmonic absorber, *Phys. Rev. B: Condens. Matter Mater. Phys.*, 2011, **84**, DOI: 10.1103/PhysRevB.84.075102.
52 D. Wernham and A. Piegari, *Optical Thin Films and Coatings*, Elsevier, 2018, pp. 789–811.
53 European Cooperation for Space Standardization (ECSS), ECSS-Q-ST-70-04C: Thermal testing for the evaluation of space materials, processes, mechanical parts and assemblies, ECSS Secretariat (ESA-ESTEC), Noordwijk, Netherlands, 2008.
54 B. N. Bhat, *Aerospace Materials and Applications*, American Institute of Aeronautics and Astronautics, Inc, Reston VA, 2018.
55 European Cooperation for Space Standardization (ECSS), ECSS-E-ST-10-03C Rev.1: Testing, ECSS Secretariat (ESA-ESTEC), Noordwijk, Netherlands, 2022.
56 NASA Goddard Space Flight Center, GSFC-STD-7000B: General Environmental Verification Standard (GEVS) for GSFC Flight Programs and Projects, Greenbelt, MD, USA, 2021.
57 Y. Yamamura and H. Tawara, Energy dependence of ion-induced sputtering yields from monatomic solids at normal incidence, *At. Data Nucl. Data Tables*, 1996, **62**, 149–253.
58 European Cooperation for Space Standardization (ECSS), ECSS-Q-ST-60-15C Rev.1: Space product assurance – Radiation hardness assurance – EEE components, ECSS Secretariat (ESA-ESTEC), Noordwijk, Netherlands, 2024.
59 J. A. Dever, A. J. Pietromica, T. J. Stueber, E. A. Sechkar and R. K. Messer, Simulated Space Vacuum Ultraviolet (VUV) Exposure Testing for Polymer Films, 39th Aerospace Sciences Meeting and Exhibit AIAA Paper 2001–1054, 2002, https://ntrs.nasa.gov/citations/20020039136.
60 C. Yan, J. Li, Y. Dai, Z. Lan, H. Wang, H. Tong, X. Ye, X. Yuan, C. Liu and H. Li, Fabrication of high-performance ALD-$Al_2O_3$/$SiO_2$ nanolaminate coating for atomic oxygen erosion resistance on polyimide, *Surf. Coat. Technol.*, 2025, **502**, 131960.
61 ASTM E21 Committee, *ASTM E595-15, Standard Test Method for Total Mass Loss and Collected Volatile Condensable Materials from Outgassing in a Vacuum Environment*, ASTM International, West Conshohocken, PA, 2015.
62 T. K. Minton, B. Wu, J. Zhang, N. F. Lindholm, A. I. Abdulagatov, J. O'Patchen, S. M. George and M. D. Groner, Protecting polymers in space with atomic layer deposition coatings, *ACS Appl. Mater. Interfaces*, 2010, **2**, 2515–2520.

 

63 A. Ioffe, L. Stil'bans, E. K. Iordanishvili, T. S. Stavitskaya, A. Gelbtuch and G. Vineyard, Semiconductor Thermoelements and Thermoelectric Cooling, *Phys. Today*, 1957, **12**, 42, DOI: 10.1063/1.3060810.

64 I. T. Witting, T. C. Chasapis, F. Ricci, M. Peters, N. A. Heinz, G. Hautier and G. J. Snyder, The Thermoelectric Properties of Bismuth Telluride, *Adv. Elect. Mater.*, 2019, **5**, DOI: 10.1002/aelm.201800904.

65 S. K. Mishra, S. Satpathy and O. Jepsen, Electronic structure and thermoelectric properties of bismuth telluride and bismuth selenide, *J. Phys.: Condens. Matter*, 1997, **9**, 461–470.

66 *Handbook of Optical Constants of Solids*, ed. E. D. Palik, Acad. Press, Boston, 1991.

67 P. B. Johnson and R. W. Christy, Optical Constants of the Noble Metals, *Phys. Rev. B: Condens. Matter Mater. Phys.*, 1972, **6**, 4370–4379.